Study of the Reactivity Mechanism of $M_3B_2O_6$ (with M = Co, Ni, and Cu) toward Lithium

A. Débart,*,† B. Revel,‡ L. Dupont,† L. Montagne,§ J.-B. Leriche,† M. Touboul,† and J.-M. Tarascon†

Laboratoire de Réactivité et de Chimie des Solides, Université de Picardie Jules Verne, UMR CNRS 6007, 33, rue St Leu, 80039 Amiens Cedex, France, Centre Commun de Mesures RMN, Université des Sciences et Technologies de Lille, 59655 Villeneuve d'Ascq Cedex, France, and Laboratoire de Cristallochimie et Physicochimie du Solide, Ecole Nationale Supérieure de Chimie de Lille, Université des Sciences et Technologies de Lille, UMR CNRS 8012, 59655 Villeneuve d'Ascq Cedex, France

Received April 16, 2003. Revised Manuscript Received July 2, 2003

The electrochemical reactivity mechanism of $M_3B_2O_6$ (with M = Co, Ni, and Cu) powders toward lithium was studied by a combination of transmission electron microscopy (TEM), infrared spectroscopy (IR), ^{11}B magic angle spinning nuclear magnetic resonance (MAS NMR), and electrochemical techniques. The electrochemical properties of these materials as anodes for lithium batteries were investigated and found to be similar to those of 3d-metal oxides. In fact, the reduction process of 3d-metal borates involves their decomposition in metal nanograins dispersed into a lithia matrix surrounded by an organic layer responsible for the observed extra capacity. The lithia matrix consists of a mixture of lithium oxide (Li_2O) and lithium orthoborate (Li_3BO_3). During the subsequent charge, the organic layer vanishes and the metal grains are partially or fully oxidized with the concomitant decomposition of Li_2O. The formation of Li_2O and metal nanograins during the discharge, as well as that of oxides nanograins during the following charge, were identified by HRTEM studies while Li_3BO_3 was detected by IR spectroscopy and ^{11}B MAS NMR techniques.

Introduction

We recently reported the reversible reactivity mechanism of 3d-metal oxides (CoO, NiO, and CuO) toward lithium that differs from the classical Li insertion/deinsertion or Li-alloying/dealloying reactions.[1−7] More specifically, we have shown that this new mechanism consists of the Li-driven decomposition of the metal oxide into a composite made of metallic nanograins dispersed into a Li_2O matrix with, upon subsequent charge, a reoxidation of metal into M_xO_y concomitant with the decomposition of Li_2O.

Back in 1995 the borates were identified by Idota et al.[8] as possible candidates for negative electrode materials in lithium-ion batteries. This interest is first nested in the low atomic weight of boron (specific capacity gain). Then, its high electronegativity as well as its ability to be either three- or four-oxygen coordinated offer a great variety of redox potentials for the adjunct cation. Because of environmental (no toxicity) and economic (material cost) factors, only iron borates have been widely studied versus lithium up to now.[9−13] However, such studies were complicated by the difficulties encountered in synthesizing a single-phase material, and in characterizing the amorphous phases obtained during cycling, despite Mössbauer spectroscopy studies.[13] Nevertheless, their electrochemical properties versus Li present several features similar to those obtained by our group with metal oxides, namely low potential reactivity, extra capacity, and important polarization.

With the wealth of experience acquired in the field of oxide reactivity (CoO, NiO, and CuO) toward lithium, we decided to study the borates using a combination of

* To whom correspondence should be addressed via e-mail: aurelie.debart@sc.u-picardie.fr.
† Université de Picardie Jules Verne.
‡ Centre Commun de Mesures RMN, Université des Sciences et Technologies de Lille.
§ Laboratoire de Cristallochimie et Physicochimie du Solide, Ecole Nationale Supérieure de Chimie de Lille, Université des Sciences et Technologies de Lille.

(1) Poizot, P.; Laruelle, S.; Grugeon, S.; Dupont, L.; Tarascon, J.-M. *Nature* **2000**, *407*, 496.
(2) Poizot, P.; Laruelle, S.; Grugeon, S.; Dupont, L.; Beaudoin, B.; Tarascon, J.-M. *C. R. Acad. Sci. Serie IIc* **2000**, *3*, 681.
(3) Poizot, P.; Laruelle, S.; Grugeon, S.; Dupont, L.; Tarascon, J.-M. *Ionics* **2000**, *6*, 321.
(4) Grugeon, S.; Laruelle, S.; Herrera Urbina, R.; Dupont, L.; Poizot, P.; Tarascon, J.-M. *J. Electrochem. Soc.* **2001**, *148*, A285−A292.
(5) Débart, A.; Dupont, L.; Poizot, P.; Leriche, J.-B.; Tarascon, J.-M. *J. Electrochem. Soc.* **2001**, *148*, A1266−A1274.
(6) Laruelle, S.; Grugeon, S.; Poizot, P.; Dolle, M.; Dupont, L.; Tarascon, J.-M. *J. Electrochem. Soc.* **2002**, *149*, A627−A634.
(7) Poizot, P.; Laruelle, S.; Grugeon, S.; Tarascon, J.-M. *J. Electrochem. Soc.* **2002**, *149*, A1212−A1217.
(8) Idota, Y.; Kubota, T.; Matsufuji, A.; Maekawa, Y.; Miyasaka, T. *Science Washington, DC* **1997**, *276*, 1395.
(9) Rowsell, J. L. C.; Gaubicher, J.; Nazar, L. F. *J. Power Sources* **2001**, *97−98*, 254.
(10) Rowsell, J. L. C.; Nazar, L. F. *J. Mater. Chem.* **2001**, *11*, 3228.
(11) Legagneur, V.; An, Y.; Mosbah, A.; Portal, R.; Salle, A. L. G. L.; Verbaere, A.; Guyomard, D.; Piffard, Y. *Solid State Ionics* **2001**, *139*, 37.
(12) Ibarra Palos, A.; Morcrette, M.; Strobel, P. *J. Solid State Electrochem.* **2002**, *6*, 1348.
(13) Ibarra Palos, A.; Darie, C.; Proux, O.; Hazemann, J. L.; Aldon, L.; Jumas, J. C.; Morcrette, M.; Strobel, P. *Chem. Mater.* **2002**, *14*, 1166.

10.1021/cm030057v CCC: $25.00
Published on Web 08/23/2003

various techniques to check whether the mechanism proposed for the oxide could be blindly extrapolated to the borates. To identify the implied electrochemical mechanism, the cycled materials were characterized by in situ X-ray diffraction (XRD), transmission electron microscopy (TEM), infrared spectroscopy (IR), and ^{11}B magic angle spinning nuclear magnetic resonance (MAS NMR).

Although $^{6,7}Li$ NMR is the most widely practiced within the field of lithium battery research,[14] we will demonstrate through this work the merits of boron NMR to identify the type of amorphous phases formed during the electrochemical reactivity of borates toward Li.

For reasons of clarity, the paper will be organized as follows. We will first exhibit the synthesis method of $M_3B_2O_6$ compounds, then their electrochemical performances together with the characterization of the cycled products, and finally we will present the NMR data.

Experimental Section

Characterization Techniques. X-ray powder patterns were collected with a Philips PW1710 diffractometer using Cu Kα monochromatic radiation, and the cell parameters were refined using Fullprof software.[15] Textural and microstructural characterizations of the powders were performed by means of conventional and high-resolution transmission electron microscopy with a Philips CM12 and a JEOL 2010 microscope, respectively. Both microscopes are equipped with in-house designed sample holders enabling investigations of moisture-sensitive samples without any air exposure. Infrared spectra were recorded on a Nicolet 510 FT-IR spectrometer with a wavenumber resolution of 1 cm^{-1} at room temperature. KBr windows were used with a similar window being placed in the reference beam in all experiments. ^{11}B MAS NMR spectra were recorded on a Bruker ASX400 spectrometer operating at 128.4 MHz. A 1-μs pulse was used with a 5-s delay time. The rotation frequency was 10 kHz. The powder samples were packed into a 4-mm-diam zirconia rotor inside an argon-filled glovebox. No change in the NMR signal was observed even for rotors left out of the drybox for several days, indicating a satisfactory airtightness. The rotors are filled to completion with dry silica to facilitate spinning and improve the field homogeneity, as they may exhibit metallic or paramagnetic properties. The chemical shifts of ^{11}B nuclei are given relative to BPO_4 at −3.6 ppm, used as a secondary reference versus $BF_3{\cdot}(C_2H_5)_2O$ at 0 ppm. The ^{11}B spectra have been fitted with the DMFIT software.[16]

Synthesis. Transition metal borates were obtained by two methods. First $M_3B_2O_6$ phases with M = Co or Cu were synthesized by solid-state reaction; respective stoichiometric mixtures of corresponding nitrates $Co(NO_3)_2{\cdot}6H_2O$ and $Cu(NO_3)_2{\cdot}3H_2O$, and boric acid (H_3BO_3) were placed into an alumina crucible that was put into an oven whose temperature was raised to 600 °C at a rate of 5 °C·min^{-1}, and maintained at this temperature for 2 d. Afterward, the samples were reground, pressed into pellets, and heated at 900 °C for 2 extra d. As determined by XRD, the obtained purple $Co_3(BO_3)_2$ powder crystallized in the kotoite-type structure (space group *Pnmn*),[17] while the $Cu_3B_2O_6$ dark green powder could be indexed on the basis of a triclinic cell with the following set of unit cell parameters: a = 3.3863(6) Å, b = 19.771(3) Å, c = 19.766(4) Å, α = 88.54(1)°, β = 69.72(1)°, γ = 69.31(1)°, space group $P\bar{1}$; in agreement with those reported in the literature for $Cu_{15}(B_2O_5)_2(BO_3)_6O_2$.[18]

The second synthesis route used namely for the elaboration of $M_3(BO_3)_2$ was a solution method based on H. Gode and A. Kešans previous studies.[19] It consists of a direct precipitation of Mn/Co/Ni-based precursors from boric acid supersaturated solutions. More specifically for the synthesis of $Ni_3B_2O_6$, 1.2 g of $NiCl_2{\cdot}6H_2O$ was dissolved in 25 mL of H_2O. A solution (25 mL of H_2O) of 1.1 g of Borax and 1.2 g of boric acid as Ni-based solution was added. A spontaneous precipitation occurred leading to an amorphous compound that was recovered by centrifugation, washed several times with distilled water and once with acetone, prior to being dried at 55 °C. The resulting green powder was annealed at 800 °C for a few days to obtain the $Ni_3B_2O_6$ phase with a kotoite-type structure, too.[17,20]

Electrochemistry. Electrochemical experiments were performed using Swagelok-type cells.[21] The positive electrode was usually prepared by mixing $M_3B_2O_6$ powder with 15% (in weight) carbon black (SP from MMM, Belgium). Amounts of mixed powders ranging from 10 to 12 mg were placed on top of the Swagelok plunger. Glass fiber disks soaked in 1 M $LiPF_6$ ethylene carbonate (EC) dimethyl carbonate (DMC) electrolyte solution were used as separators between the positive and lithium foil negative electrodes. Room-temperature galvanostatic cycling was performed within a 0.02−3 V range at C/5 rate (C being defined as 1 Li+ exchanged in 1 h) by means of a Mac Pile system (Biologic S. A., Claix, France), unless otherwise specified. After cycling, the cells were disassembled in a glovebox. The recovered powder was then washed with pure DMC to remove electrolyte traces, prior to being characterized by TEM, infrared spectroscopy, and ^{11}B magic angle spinning nuclear magnetic resonance measurements.

Results and Discussion

Electrochemical Tests. The voltage−composition curves for $M_3B_2O_6$/Li half cell with M = Co, Ni, Cu shows, during the first discharge, well-defined plateaus located at 0.95 V for $Co_3B_2O_6$ (Figure 1), 1.05 V for $Ni_3B_2O_6$ (Figure 2), and 2.05 V for $Cu_3B_2O_6$ (Figure 3), which are visualized on the differential capacity plots (insets of Figures 1, 2, and 3, respectively). Note that for the peculiar $Li_xCo_3B_2O_6$ curve, two extra plateaus at 1.25 and 1.05 V are observed (black arrows on Figure 1) whose origin has not yet been identified. Interestingly, the borate reduction potentials are systematically higher than those measured for metal oxides under similar conditions. The $V = f(x)$ curves are recorded for the corresponding oxides on Figures 1, 2, and 3. Such observed difference is simply rooted in the boron inductive effect as compared to oxygen.

The full reduction of M^{2+} into M^0 during the electrochemical discharge of $M_3B_2O_6$ will require six lithiums per unit formula; but, whatever the nature of M, we measured the reactivity of about 7.8 lithiums, implying an extra capacity of 1.8 lithiums. The Li reactivity process is not fully reversible, because out of the 7.8 lithium ions reacted in the first discharge, only 3.8, 5, and 3.4 can be removed in the subsequent charge for $Co_3B_2O_6$, $Ni_3B_2O_6$, and $Cu_3B_2O_6$ materials, respectively,

(14) Menetrier, M.; Saadoune, I.; Levasseur, S.; Delmas, C. *J. Mater. Chem.* **1999**, *9*, 1135.
(15) Rodriguez-Carvajal, J. *Collected Abstracts of Powder Diffraction Meeting*; Galy, J., Ed.; Toulouse: France, July 1990; p 127.
(16) Massiot, D.; Fayon, F.; Capron, M.; King, I.; Le Calve, S.; Alonso, B.; Durand, J. O.; Bujoli, B.; Gan, Z. H.; Hoatson, G. *Magn. Reson. Chem.* **2002**, *40*, 70.
(17) Effenberger, H.; Pertlik, F. *Z. Kristallogr.* **1984**, *166*, 129.
(18) Behm, H. *Acta Crystallogr.* **1982**, *B38*, 2781.
(19) Kešans, A. D.; Gode, G. K. *Chemistry of Borates*; *Akad. Nauk SSSR, Neorg. Mater.*, 1953; ch. Synthèses de borates en solutions aqueuses, pp 29−43.
(20) Pardo, J.; Martinez-Ripoll, M.; Garcia-Blanco, S. *Acta Crystallogr.* **1974**, *B30*, 37.
(21) Guyomard, D.; Tarascon, J.-M. *J. Electrochem. Soc.* **1992**, *139*, 937.

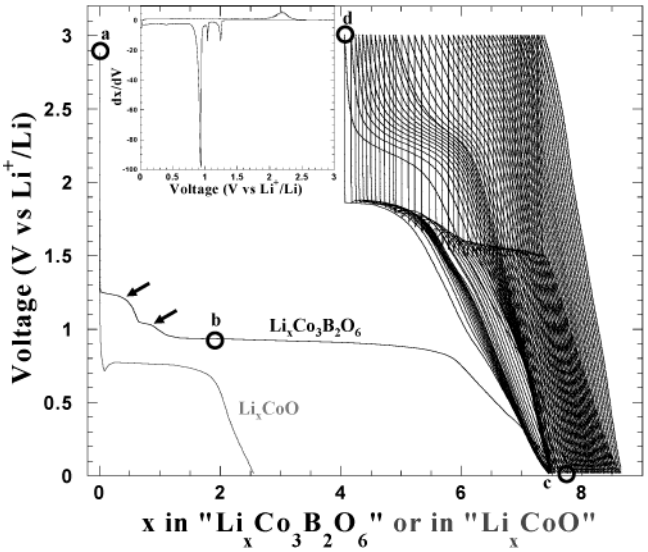

Figure 1. Voltage−composition curves realized on $Li/Co_3B_2O_6$ (black curve) and Li/CoO (gray curve) cells cycled at C/5 rate. The inset corresponds to the voltage−composition derivative trace. The black arrows indicate two extra plateaus, and letters a, b, c, and d point out the TEM and infrared spectroscopy studied samples.

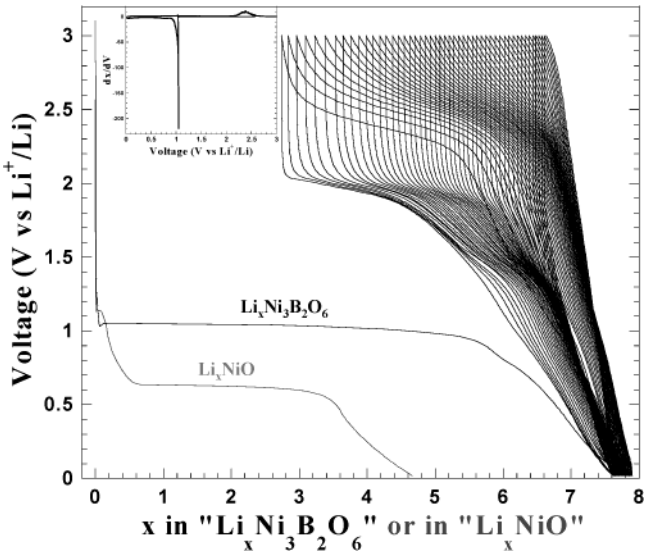

Figure 2. Voltage−composition curves for $Li/Ni_3B_2O_6$ (black curve) and Li/NiO (gray curve) cells cycled at C/5 rate together with, as an inset, the differential voltage−composition trace for the same cell.

leading to capacities of about 700 mAh/g that decay to 300 mAh/g on subsequent cycles. By comparison with our previous works on oxides, we should note that both the irreversible capacity between the first discharge and charge and the capacity retention are worse for the borates than for the oxides. In contrast, the extra-capacity per 3d metal is of the same amplitude (0.6 per 3d metal).

Thus, to throw some light on the origin of the above-mentioned differences, we began on a thorough study of the mechanisms involved during the Li reaction with $M_3B_2O_6$ by means of in situ X-ray diffraction, TEM, infrared spectroscopy and ^{11}B magic angle spinning nuclear magnetic resonance measurements.

In situ X-ray Diffraction Study. In situ XRD patterns were obtained by means of an electrochemical

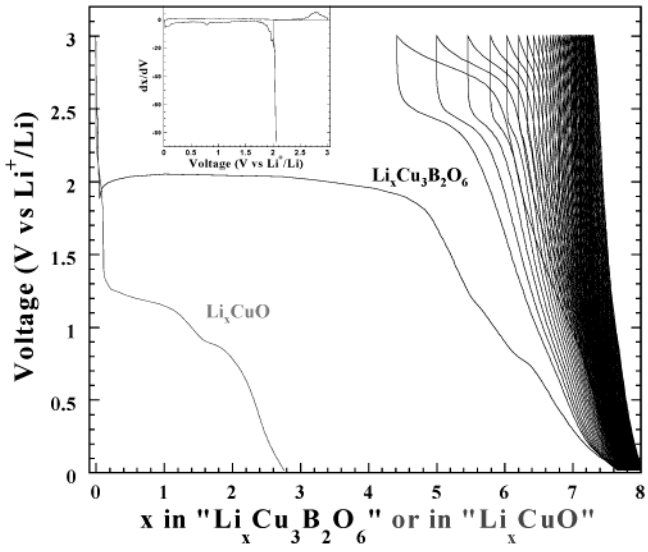

Figure 3. Voltage−composition curves realized on $Li/Cu_3B_2O_6$ (black curve) and Li/CuO (gray curve) cells cycled at C/5 rate. The inset corresponds to the differential capacity vs voltage for the same $Li/Cu_3B_2O_6$ cell cycled between 3 and 0.02 V at C/5.

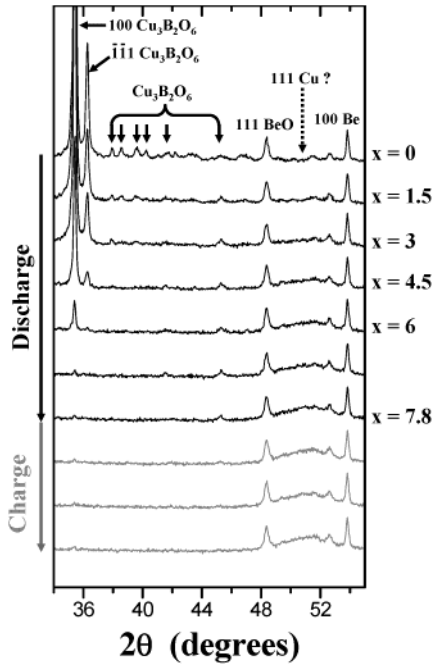

Figure 4. In situ X-ray diffraction performed on a $Li/Cu_3B_2O_6$ electrochemical cell cycled at C/5. Black XRD patterns were taken during the first discharge and the gray ones were recorded during the following charge.

cell (assembled similarly to our Swagelok cell but having a beryllium window as current collector on the positive electrode side) that was placed on a D8-Bruker diffractometer (CoKα radiation, PSD counter) operating in θ/θ geometry. The cell was connected to a Mac-pile system operating in a galvanostatic cycling mode using current equivalent to a C/5 rate. For reasons of clarity, we will present each case separately.

In situ X-ray Diffraction Study of $Cu_3B_2O_6$. During the first discharge a continuous decrease in the $Cu_3B_2O_6$ Bragg peaks intensity was observed up to $x = 6$ (Figure 4), leading to a featureless XRD pattern that did not really evolve upon further reduction and subsequent

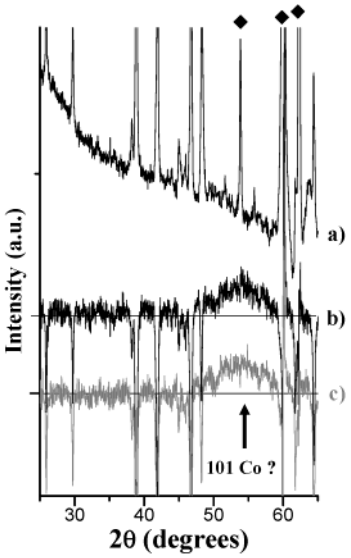

Figure 5. In situ X-ray diffraction carried out on a Li/$Co_3B_2O_6$ cell. For $x = 0$ (a), the black lozenges indicate the cell peaks. (b) Black curve obtained by subtracting the X-ray diagrams of the initial sample from the fully discharged one. (c) Grey curve obtained by plotting the subtracted difference between the initial and charged X-ray diagrams for $Co_3B_2O_6$ samples. A black arrow indicates the major metallic cobalt reflection (d(101)Co).

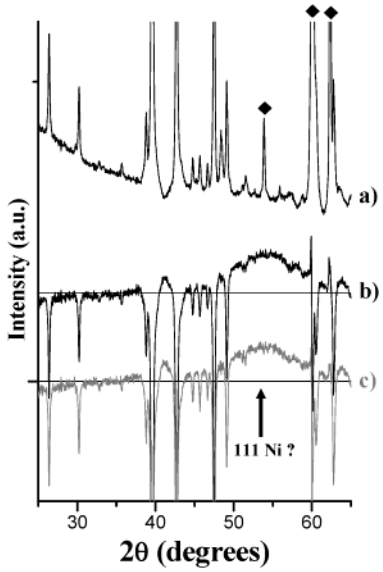

Figure 6. In situ X-ray diffraction carried out on a Li/$Ni_3B_2O_6$ cell. For $x = 0$ (a), the black lozenges indicate the cell peaks. (b) Black curve obtained by subtracting the X-ray diagrams of the initial sample from the fully discharged one. (c) Gray curve obtained by plotting the subtracted difference between the initial and charged X-ray diagrams for $Ni_3B_2O_6$ samples. A black arrow indicates the most important metallic nickel reflection (d(111)Ni).

oxidation. Only one weak and broad reflection located at a 2θ value of 50.7° ($d = 2.09$Å) appeared on deep discharge (black XRD patterns on Figure 4), and was preserved upon the following charge (gray XRD patterns). This d value corresponds to the main metallic copper reflection (d(111)Cu). Nevertheless, assigning this peak to a Cu phase is difficult because only one reflection is observed.

In situ X-ray Diffraction Study of $Co_3B_2O_6$. The in situ X-ray diagram of initial $Co_3B_2O_6$ sample is shown on Figure 5a. To better highlight the differences, the XRD patterns for the discharged (Figure 5b) and charged (Figure 5c) samples were obtained by subtracting the initial $Co_3B_2O_6$ X-ray diagram. During the first discharge, the $Co_3B_2O_6$ X-ray peaks disappear (their intensities are observed as negative on Figure 5b), and only one broad and weak reflection emerges at a 2θ value of 55.8° ($d = 1.91$ Å) that may correspond to the major hexagonal metallic cobalt reflection (d(101)Co). Upon the following charge, almost no change is observed on the X-ray pattern difference (Figure 5c), only the intensity of the remaining broad peak seems to slightly decrease within the accuracy of the measurements.

In situ X-ray Diffraction Study of $Ni_3B_2O_6$. The same trends are observed as for the lithiated or delithiated copper or cobalt phases. During the discharge, the $Ni_3B_2O_6$ Bragg peaks vanish (Figure 6b) and one wide reflection located at a 2θ value of 52.2° ($d = 2.03$ Å), which corresponds to the (111) metallic nickel reflection, appears. Upon the following charge its intensity seems to slightly decrease (Figure 6c).

In short, for the three studied compounds, once the first discharge is achieved, there is a disappearance of all Bragg peaks, corresponding to the starting material, to the expense of only one diffuse and poorly resolved Bragg peak most likely indicative of the presence of metallic elements. On the subsequent charge, this broad observed peak seems to decrease in intensity, suggesting that a small part of the metal could be reoxidized (as already reported in the transition metal oxides studies). Nevertheless, using X-ray diffraction, besides the weak evidence for the presence of metallic element, we failed to identify the nature of the fully reduced or reoxidized phases; hence the need to pursue TEM studies.

TEM Study. We will present the results by treating separately the most relevant domains of the voltage−composition curve during the first discharge/charge that will be referred to by letters **a** to **d** on the curve (Figure 1). The reactivity scheme common to all borates will first be exposed and then a specific observation for each transition metal borate will be given.

The starting $Li_xM_3B_2O_6$ ($x = 0$; Figure 1, point a) powders are crystallized, monolithic, and composed of well-defined plates, characteristic of the ceramic materials (figures are not presented).

For all of the studied borates, the reduction by Li up to $x = 2$ leads to the appearance of a voltage plateau on the discharge curve (Figure 1, point b). TEM imaging and SAED techniques indicate that such a plateau is associated with a phase decomposition (Figure 7a−c, d−f, and g−i for M = Co, Ni, Cu, respectively). For each $x = 2$ compound, the starting platelets are fully or partially disintegrated into nanoparticles (Figure 7a, d, and g). This textural transformation is associated with a structural modification that could be easily observed on SAED patterns (Figure 7b, e, and h). On SAED patterns, punctual spots of the monolithic initial materials disappeared at the expense of diffraction rings. To clearly index each ring, the SAED patterns were treated through Process Diffraction 2.1.7. software[22] that creates an "equivalent" X-ray diffraction pattern in 2θ using CuKα monochromatic radiation (Figure 7c,

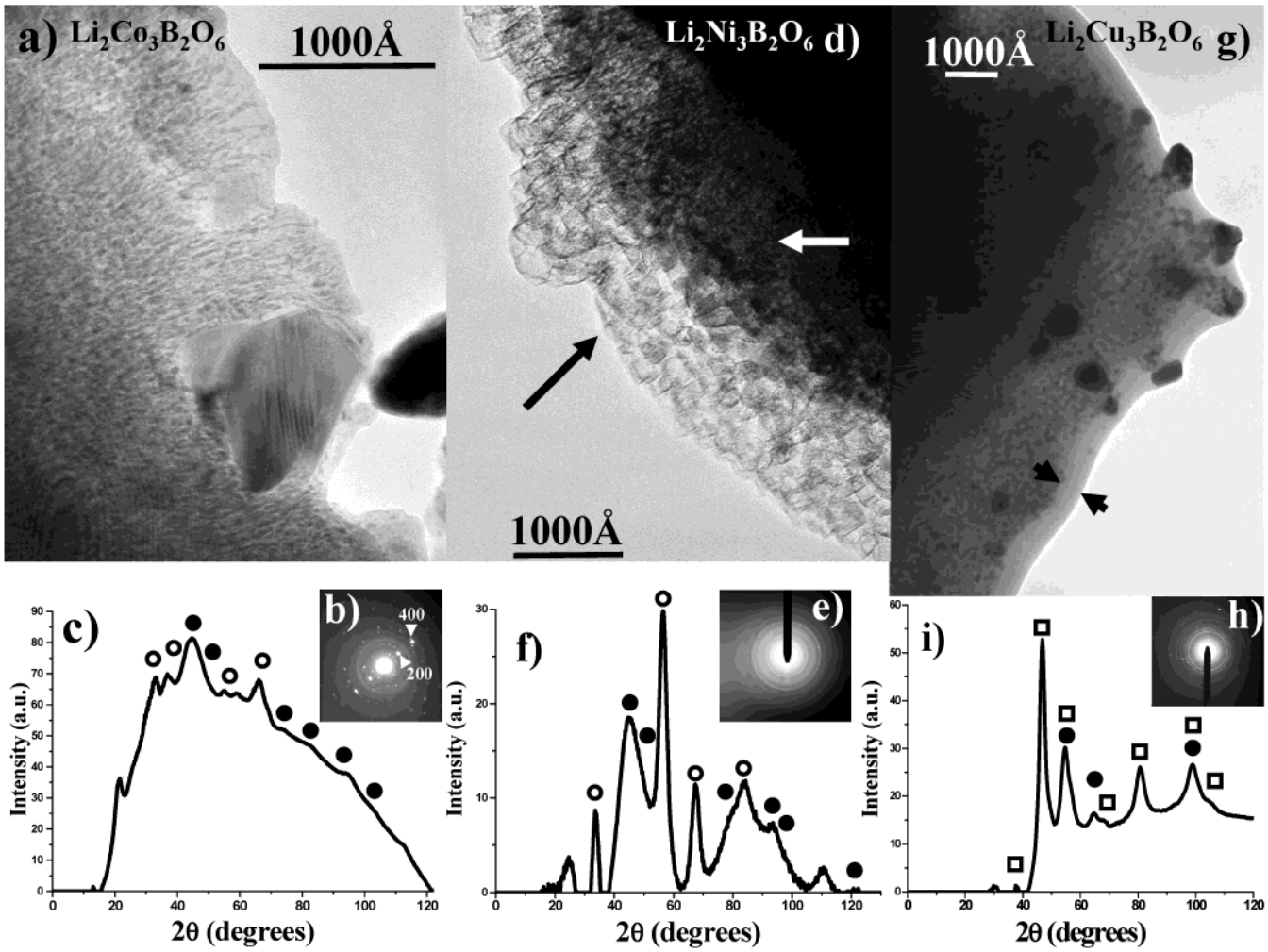

Figure 7. (a) Bright field TEM image of the "$Li_2Co_3B_2O_6$" particle. Note the disintegration of the starting platelet with formation of nanoparticles and crystals maintenance. (b) Corresponding SAED patterns consist of sharp spots indexed with $Co_3B_2O_6$ cell parameters and rings. (c) Corresponding XRD-like diagram obtained with Process Diffraction 2.1.7 showing that the material transforms into a phase having a Co-type structure (full dots indicate Co Bragg peaks) embedded into a Li_2O matrix (Li_2O reflections are pointed out by circles). (d) Overall image of a "$Li_2Ni_3B_2O_6$" particle showing that nanoparticles (white arrow) are surrounded by an inorganic matrix (black arrow). (e) Corresponding SAED pattern. (f) Corresponding XRD-like diagram still indexed with Ni (full dots) and Li_2O cell parameters. (g) Micrograph of a $Cu_3B_2O_6$ sample having reached the capacity of 2 lithiums showing that the initial particles are transformed into 80−100 Å nanograins with global shape particle conservation and an inorganic matrix (black arrows) surrounding the nanoparticles. (h) Corresponding SAED pattern. (i) Equivalent XRD-like diagram whose peaks are indexed with metallic copper (full dots) and Cu_2O (squares) cell parameters.

f, and i). Using JCPDS standards, the observed reflections were successfully indexed. These diagrams show that $M_3B_2O_6$ phases partly change into at least two phases; one corresponding to the metallic element (represented by full dots) and the other corresponding to Li_2O (indicated by circles, Figure 7c and f). These results are consistent with those obtained for oxides with namely the appearance of metallic nanoparticles embedded into the Li_2O matrix during cell discharge. Nevertheless, with the metal transition borates, some specific differences that were the most pronounced for "$Li_xNi_3B_2O_6$" were observed. Indeed in contrast with the oxides, the Li_2O matrix is not amorphous but rather made of very thin platelets with sharp edges overlapping, and whose size could exceed several hundreds of angstroms (Figure 8a). The Li_2O domain size is so big that it is almost possible to isolate one of these domains to obtain a punctual SAED pattern (Figure 8b) indicating that these crystallites are lying down on the $(02\bar{2})$ plane. Thus, a legitimate question is why did not we observe Li_2O by X-rays (Figure 6b)? A possible reason might be the large difference between the X-ray scattering of Li_2O (made of light elements) as compared to heavy elements such as 3d metals. On the contrary, for the copper borate, it is the inorganic layer (classified as inorganic because it was hardly resistant to the beam intensity) that is clearly visible on the micrograph (black arrows on Figure 7g) after only 2 lithium ions are inserted, but it seems to be amorphous on the SAED pattern (Figure 7h−i) similar to what we observed at the beginning of Li/CuO discharge.[5] This layer is more than one hundred angstroms thick, and it was measured to have a maximum width of 30 Å in the case of oxides studies.[5] Note that for both cobalt and copper borates, $M_3B_2O_6$ large domains of more than 500 Å (compare to

(22) Lábár, J. L. *Proceedings of the European Congress on Electron Microscopy (EUREM) 12*; Frank, L., Ciampor, F., Eds.; Brno, Czech Republic, July 2000; p 1379.

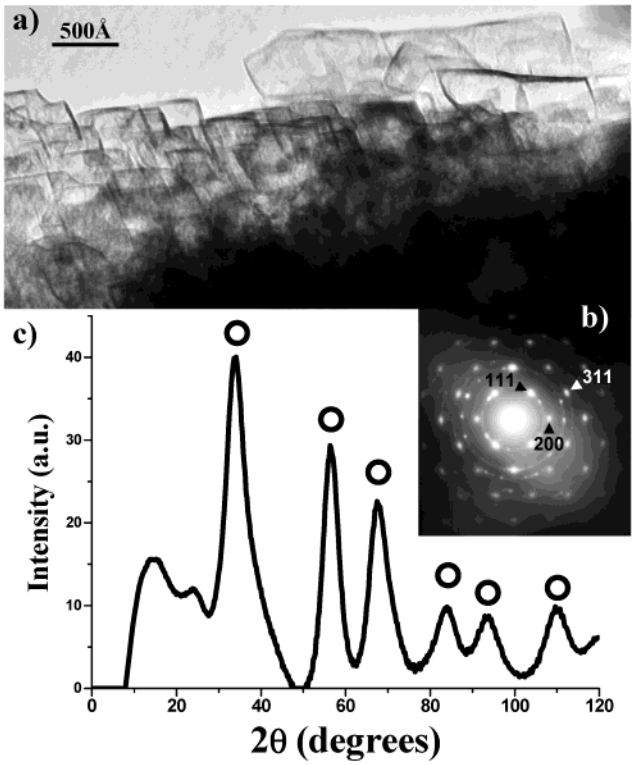

Figure 8. (a) Bright field TEM image of the inorganic matrix that grows on "$Li_2Ni_3B_2O_6$" particles surface upon discharge. (b) Corresponding SAED pattern composed of both rings and spots highlighting the matrix good cristallinity. (c) Matching XRD-like diagram points out that the sets of rings as well as the spots can be indexed with Li_2O cell parameters (circles).

metallic nanograins) are still observed. Finally, the last point concerns the indexing of the SAED pattern recorded on partially discharged copper borate (Figure 7i). Only Cu_2O (squares) and metallic copper (full dots) reflections are observed, showing first that the reduction of Cu(II)/Cu(I) and Cu(I)/Cu metal occurs at the same potential (2.05 V), whereas Cu_2O is classically reduced into copper at 1.35 V.[4]

Afterward, $Li_xM_3B_2O_6$ samples were studied after a full discharge (Figure 1, point c). During the first discharge, $M_3B_2O_6$ was disintegrated into metal nanoparticles embedded in a Li_2O matrix, (Figure 9a−j) and surrounded by an organic and amorphous layer (Figure 9i), as for metal oxides.[1−7] This layer was observed to quickly decay under the electron beam, suggesting its organic nature. Interestingly, among the borate family, as previously observed before with the oxides,[1−7] the metal size of nanoparticles upon reduction by Li is always smaller for the Co-based phase (30 Å) as compared to 50 Å and 80 Å for Ni- and Cu-based phases, respectively (Figure 9a, d, and j). It seems that whatever the starting material is (borate, oxide, nitride, fluoride, or phosphide),[4,5,7,23,24] the size of reduced nanograins is linked to the nature of the transition metal (30 Å for Co, 50 Å for Ni, and 80 Å for Cu). However, we did not succeed in spotting any evidence for the presence of boron-based phases in either of the reduced composites.

Moreover, during the reoxidation (Figure 1, point d), like for the oxides, the "organic" layer vanishes first. Then, only a partial reoxidation into oxide is observed according to SAED patterns and corresponding XRD-like diagrams (Figure 10b−c, e−f, and h−i). For instance, a SAED pattern of fully reoxidized $Cu_3B_2O_6$ sample (Figure 10h) reveals two sets of rings indicating the coexistence of at least Cu (full dots) and Cu_2O (squares) phases (Figure 10i) while SAED patterns of fully reoxidized $Co_3B_2O_6$ and $Ni_3B_2O_6$ samples show that the electrode material is made of at least a mixture of MO (triangles), metal (full dots), and Li_2O (circles) (Figure 10b−c and e−f), without any evidence for the presence of a crystallized boron phase. Reflections due to metals are still observed at 3 V. The poor reoxidation of the nanoparticles explains the strong capacity loss observed on the voltage vs composition curve presented in Figures 1−3 between the first discharge and charge.

Although the TEM study does not give any clues on the outcome of boron, it demonstrates that the electrochemical reactivity of these borates as anode for lithium batteries is, to a certain extent, similar to that of 3d-metal oxides. During reduction, $M_3B_2O_6$ decomposes into metal nanoparticles embedded in a Li_2O matrix, and surrounded by an organic and amorphous layer, responsible for the extra capacity. Afterward in the course of oxidation, the "organic" layer vanishes and the metal is partially reoxidized. Nevertheless, the oxides have a better reversibility toward lithium than the borates do, this effect being most likely nested in the morphology of the Li_2O phase. Li_2O particles will lead to the expectation of poor kinetics and therefore a poor conversion process, as we observed.

However, quite disturbing is the fact that, while present in the electrode material, we could not observe boron by TEM techniques, suggesting that either we had eliminated the boron-based phases during the washing process or most likely that amorphous boron-based phases were forming. As an attempt to distinguish between these two possibilities, IR spectroscopy was performed.

IR Spectroscopy. With regard to structure, the kotoite-type structure compounds ($Co_3B_2O_6$ and $Ni_3B_2O_6$) can be viewed as consisting of monoborate group (BO_3), whereas the $Cu_3B_2O_6$ structure consists of almost planar B_2O_5 and BO_3 groups, with the latter being isolated. Thus, strictly speaking, $Co_3B_2O_6$ and $Ni_3B_2O_6$ are both bismonoborate, whereas $Cu_3B_2O_6$ is a bisdiborate hexamonoborate dioxide ($Cu_{15}(B_2O_5)_2(BO_3)_6O_2$). Such differences imply drastic dissimilarities between the infrared spectra, that of copper borate is more complex than those of kotoite-type materials.[25] For an isolated, planar, trigonal BO_3 group of D_{3h} symmetry, the expected vibration modes positions are $\nu_1 = 750$ cm^{-1} and $\nu_2 = 1250$ cm^{-1}, and are somewhat changing with the crystal field, the reason they are lightly shifted for the metal borates. Interestingly, however, they shift during cycling toward such positions as expected for the BO_3 group, indicative of the disappearance of the crystal field as expected in the case of decomposed matter. There is no actual evolution for the kotoite-type structure compounds (their spectra are not shown), whereas in the

(23) Pereira, N.; Dupont, L.; Tarascon, J.-M.; Klein, L. C.; Amatucci, G. G. *J. Electrochem. Soc.* **2003**, *150*, A1273.
(24) Grugeon, S.; Laruelle, S.; Dupont, L.; Tarascon, J.-M. *Solid State Sci.* **2003**, *5*, 895.
(25) Weir, C. E.; Schroeder, R. A. *J. Res. Nat. Bur. Stand.* **1964**, *68A*, 465.

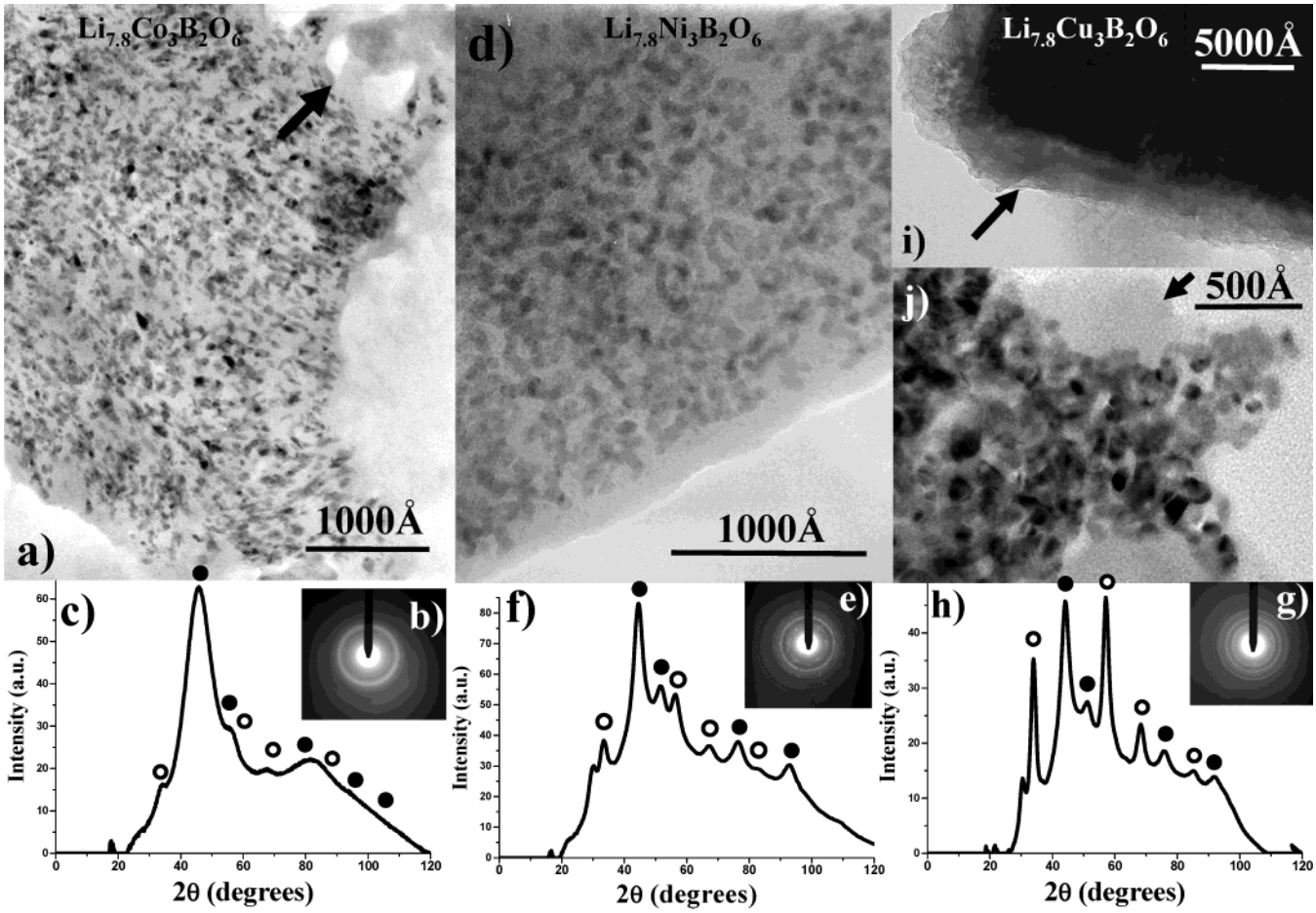

Figure 9. (a) Micrograph of a fully reduced $Co_3B_2O_6$ material. (b) Corresponding SAED pattern. (c) Involved XRD-like diagram showing, by comparison with the previous one (7c), that the physicochemical nature of the nanoparticles embedded in the matrix (black arrow) does not change. (d) Bright field TEM image of the totally reduced $Ni_3B_2O_6$ powder. (e) Corresponding SAED pattern. (f) Produced XRD-like diagram still indexed with Ni (full dots) and Li_2O (circles always indicate Li_2O Bragg peaks) phases as the previous one (7f). (g) SAED pattern of a completely reduced $Cu_3B_2O_6$ material. (h) Equivalent XRD-like diagram whose rings are indexed with metallic copper (full dots) and Li_2O phases revealing that the "organic" layer observed on the image (i) is amorphous. (i) Image of a part of the sample showing the amorphous coating ("organic" layer) indicated by a black arrow embedding the nanograins. (j) Bright field HRTEM image of the totally reduced $Cu_3B_2O_6$ material where metallic copper nanograins are observed embedded in the inorganic matrix (black arrow) and the e-beam drive "organic" layer melting.

case of $Cu_3B_2O_6$, the bands of the B_2O_5 group, whose positions are indicated by the broken arrows on Figure 11, disappear in the course of cycling (Figure 11b−e). Simultaneously, the bands of the BO_3 group (continuous arrows) become more distinct for cycling.

In short, IR spectroscopy demonstrates that there is no solubilization of the borate during cycling, and in addition that the so-obtained phase is composed of simple isolated planar trigonal BO_3 group. Therefore, to characterize the redox products, and to fully identify the existing boron phase, ^{11}B magic angle spinning nuclear magnetic resonance was used.

^{11}B Magic Angle Spinning Nuclear Magnetic Resonance Study. Paramagnetic, ferromagnetic, and anti-ferromagnetic phases, that is to say those containing (Co^{2+}, Cu^{2+}), (Co^0, Ni^0), and (NiO, and CoO), respectively, in this present case, could not be observed by ^{11}B MAS NMR. Consequently, only cycled $Cu_3B_2O_6$ samples were studied. The NMR spectra of reduced and oxidized $Cu_3B_2O_6$ samples (Figure 12b−c) are characteristic of nuclei affected by the second-order quadrupolar broadening, in accordance with the 3/2 nuclear spin of ^{11}B. The fitting of the line indicates the presence of only one site with a chemical shift of 21.9 ppm (corrected from quadrupolar induced shift), together with a quadrupolar constant (Cq) of 2.7 MHz, and a quadrupolar symmetry constant (η_q) of 0.15. These NMR parameters are in accordance with the presence of tricoordinated borons.[26] We notice that the spectra have a broad line shape as compared to the crystalline reference Li_3BO_3 (Figure 12a), which is indicative of an amorphous material. By comparison with crystalline reference compounds,[26] we found that the NMR parameters of reduced and oxidized $Cu_3B_2O_6$ samples (Figure 12b−c) are similar to those of boric acid (H_3BO_3) or lithium orthoborate (α-Li_3BO_3)[27] (Figure 12a). Spectra recorded with and without proton decoupling did not show any difference, meaning that no protons are attached to the boron nuclei in our samples, therefore we deduced that the spectra in Figure 12b−c are characteristic of the presence of lithium orthoborate (α-Li_3BO_3). We could unambiguously conclude that the borate phase created during cycling is lithium ortho-

(26) Mackenzie, K. J. D.; Smith, M. E. *Multinuclear Solid State NMR of Inorganic Materials*; Cahn, R. W., Ed.; Pergamon Materials Series; Pergamon Press: Elmsford, NY, 2002; Vol. 6.

(27) Takahashi, M.; Toyuki, H.; Tatsumisago, M.; Minami, T. *Solid State Ionics* **1996**, *86−88*, 535.

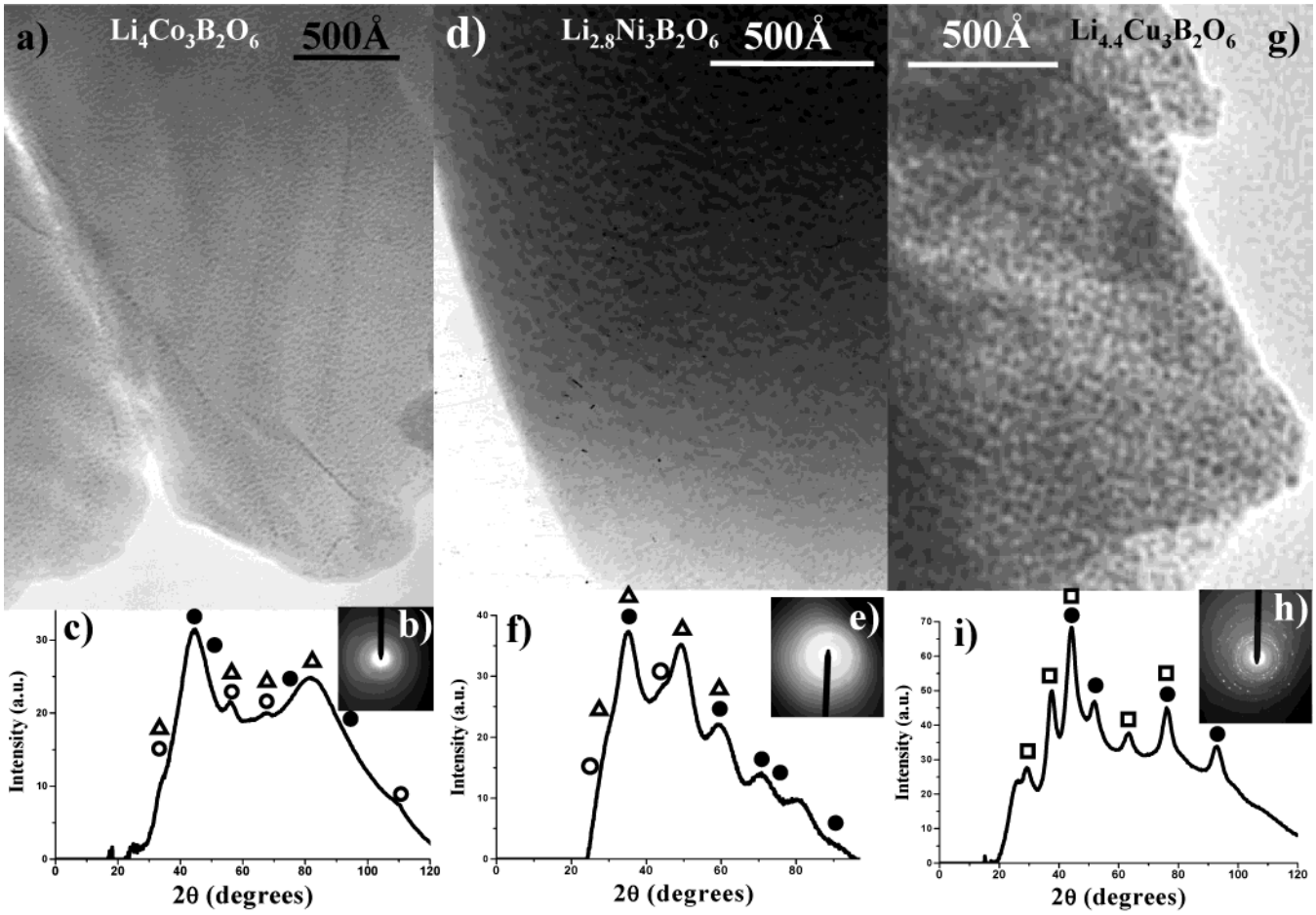

Figure 10. (a) Bright field image of a fully reoxidized $Co_3B_2O_6$ sample. (b) Corresponding SAED pattern. (c) Corresponding XRD-like diagram showing a partial reoxidation of Co metal (full dots) into CoO (triangles), and the Li_2O subsistence (circles). (d) Micrograph of a fully reoxidized $Ni_3B_2O_6$ sample. (e) Corresponding SAED pattern. (f) Matching XRD-like diagram showing that the sets of rings are indexed with metallic nickel (full dots), NiO (triangles), and Li_2O (circles). (g) Bright field image of an entirely reoxidized $Cu_3B_2O_6$ sample showing that the "organic" layer has vanished. (h) Corresponding SAED pattern. (i) Resultant XRD-like diagram where Li_2O is missing while the sets of rings are indexed with Cu (full dots) and Cu_2O (squares) cell parameters.

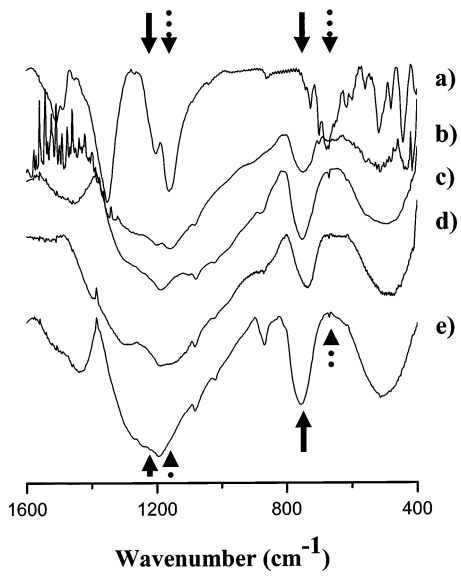

Figure 11. Infrared absorption spectra of (a) $Cu_3B_2O_6$ initial material, (b) discharged to $x = 2$, (c) discharged, (d) charged, and (e) 50 cycles (between 3 and 0.02 V at C/5) samples of $Cu_3B_2O_6$. The continuous arrows indicate bands position of BO_3 groups and the broken arrows indicate those of B_2O_5 groups.

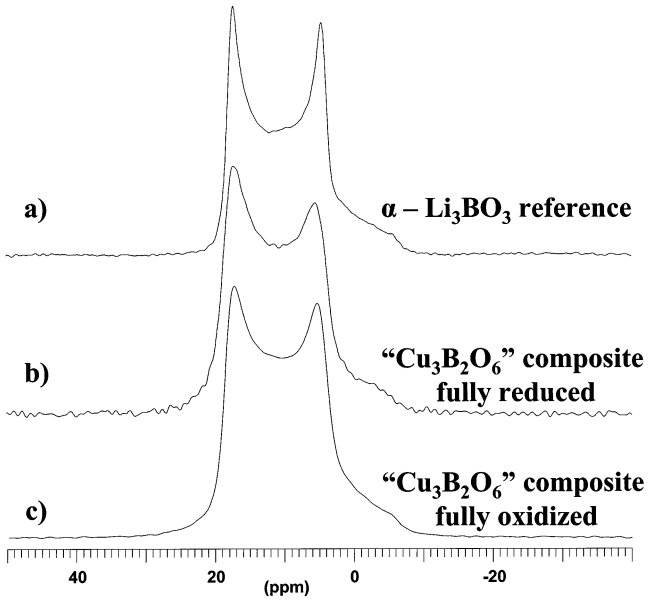

Figure 12. ^{11}B Magic angle spinning nuclear magnetic resonance spectra of (a) synthetic α-Li_3BO_3 used as standard, (b) powder recovered after full reduction of $Cu_3B_2O_6$, and (c) powder recovered after full oxidation of $Cu_3B_2O_6$.

borate. Furthermore, we should note that this phase remains unchanged upon cycling, in contrast to Li_2O.

Conclusions

A combination of TEM, IR, ^{11}B MAS NMR, and electrochemical techniques has enabled a thorough understanding of the Li reacting processes involved during the cycling of $M_3B_2O_6$ (with M = Co, Ni, and Cu) powders vs Li. To a certain extent, the Li reactivity mechanism of these borates is similar to that of the previously reported 3d-metal oxides. Therefore, a few differences in the mechanism were noted depending upon the nature of the transition metal. The main difference resides first in the formation of the Li_2O phase that does not fully decompose on the subsequent charge, and second in the growth of a borate phase that, once formed, does not evolve upon cycling. For the Co and Ni-based borates, we have found upon reduction the straight formation of metal nanograins embedded into a $Li_2O-\alpha$-Li_3BO_3 matrix surrounded by an "organic" layer, whereas for $Cu_3B_2O_6$ we have the formation of Cu_2O as an intermediate step. Such textural/compositional differences are responsible for the poor kinetic of the conversion process, therefore implying a poor reversibility and capacity retention. This clearly emphasizes the positive attribute of having a true nanocomposite for optimum performances.

Acknowledgment. We thank S. Grugeon, S. Laruelle, R. Herrera-Urbina, M. Bequerel, T. Bequerel, and M. Nelson for helpful discussions, and the CRISMAT (Caen) for enabling the HRTEM studies with special thanks to R. Retoux for his technical discussions and expertise.

CM030057V